J. Fluid Mech. (2005), vol. 523, pp. 367–392. © 2005 Cambridge University Press
DOI: 10.1017/S0022112004002344 Printed in the United Kingdom

The temporal evolution of baroclinic basin-scale waves in a rotating circular basin

By GEOFFREY W. WAKE, GREGORY N. IVEY AND JÖRG IMBERGER

Centre for Water Research, University of Western Australia, Nedlands,
Western Australia 6907, Australia

(Received 19 March 2004 and in revised form 3 September 2004)

The temporal evolution of baroclinic basin-scale waves in a rotating circular basin following an initial forcing event is investigated using a laboratory study. Experiments conducted in the circular domain containing a two-layer fluid with a flat bottom and vertical sidewalls demonstrate that the response is essentially linear with frictional effects at the boundaries steadily dissipating wave energy. Experiments conducted in the same configuration but with the addition of simple topographic features, either a radially protruding cape or a bathymetric ridge, exhibit wave/topography interactions that result in the formation of an eddy field and an offshore flow, respectively. The rate of wave decay, as well as the amount of horizontal mixing occurring within the basin, is significantly enhanced by such interactions. The results of this study are then considered in terms of their implications for the baroclinic basin-scale wave energy pathways in large stratified lakes influenced by the Earth's rotation.

---

1. Introduction

In stratified enclosed water bodies, a portion of the mechanical energy input from wind forcing generates baroclinic basin-scale waves (e.g. Csanady 1967; Antenucci & Imberger 2001; Stocker & Imberger 2003) that distribute energy throughout the domain (Gill 1982). Internal waves may transfer energy within a lake from the basin-scale to the smallest scales of motion (Saggio & Imberger 1998) and thus have the potential to affect directly the distribution of sediments, nutrients, dissolved oxygen and other biological agents within lakes (e.g. Imberger 1998). The current study investigates the temporal evolution of baroclinic basin-scale waves and those energy pathways within water bodies large enough to be influenced by the Earth's rotation.

The pioneering work on such lakes was performed by Lamb (1932) who discussed free wavelike motions in a circular domain consisting of a flat bottom and vertical sidewalls containing a single fluid layer. A subsequent study by Csanady (1967) extended these results to a two-layer fluid, whereas Antenucci & Imberger (2001) used an analytical model to investigate the ratio of kinetic to potential energy for freely evolving baroclinic basin-scale waves. Stocker & Imberger (2003) provided an analytical description of the linearized initial boundary-value problem for a surface tilt in a circular lake and quantified the amount of energy contained in the wave response due to the initial forcing. Nonlinear and frictional effects, neglected by such linear inviscid analysis, are important in the field (e.g. Martinsen & Weber 1981; Antenucci & Imberger 2001; Rueda, Schladow & Pálmarsson 2003) and are required to describe the temporal evolution of baroclinic basin-scale waves and, hence, the associated energy pathways within such systems.

Within a circular domain, nonlinear effects may manifest themselves in three basic ways. First, it has been demonstrated that the nonlinear steepening of a basin-scale wave, owing to the initial forcing and ambient stratification, results in the transfer of energy to solitary waves with a much shorter lengthscale in a non-rotating channel (Horn, Imberger & Ivey 2001; Horn *et al.* 2002). Similarly, Melville, Tomasson & Renouard (1989) have shown that, in a rotating system, nonlinear steepening of a Kelvin wave leads to the transfer of energy to Poincaré modes of the channel. Secondly, nonlinear interactions between the basin-scale modes may lead to the transfer of energy to higher modes (Riley & Lelong 2000). This process has been described in a rotating channel where nonlinear interactions between modes led to the growth of a Poincaré mode wave at the expense of two Kelvin modes (Tomasson & Melville 1990). Thirdly, the basin-scale waves may exchange energy with a background mean flow (e.g. Kuo & Polvani 1999; Riley & Lelong 2000). Theoretical studies on nonlinear geostrophic adjustment in infinite (Reznik, Zeitlin & Ben Jelloul 2001; Zeitlin, Reznik & Ben Jelloul 2003) and semi-infinite (Reznik & Grimshaw 2002) domains have demonstrated that there is no interaction between the slow (mean flow) and fast (wave) components of the response; however, in the current study the fast (basin-scale wave) response remains trapped within the bounded domain so that an exchange of energy between the basin-scale waves and a mean flow cannot be discounted.

Friction associated with the bottom and the sidewall boundaries of the circular domain influences the temporal evolution of baroclinic basin-scale waves by causing a reduction in the phase speed and a decrease in amplitude as the waves progress (e.g. Martinsen & Weber 1981).

Topography may also be important in determining the basin-scale wave energy pathways, with previous studies demonstrating that interactions between (longshore-propagating) long waves and bathymetric ridges may lead to the transmission of energy offshore, resulting in a significant reduction in the propagating wave amplitude (Killworth 1989*a*,*b*; Chang 1991). Interactions between basin-scale waves and abrupt changes in shoreline topography have resulted in flow separation and the generation of cyclonic and anticyclonic eddies at the expense of the basin-scale waves (Ivey & Maxworthy 1992). Field studies in large stratified lakes have postulated that wave/topography interactions may result in generation of meso-scale eddies (Ralph 2003) or in the steepening of the basin-scale wave front leading to the generation of high-frequency waves (e.g. Saggio & Imberger 1998; Boegman *et al.* 2003).

In the current study, we use a laboratory experiment to investigate the importance of nonlinear, frictional and topographic effects on the temporal evolution of baroclinic basin-scale waves in a rotating circular basin. In doing so, the dominant mechanisms by which baroclinic basin-scale wave energy may be transferred (owing to nonlinear or topographic interactions) or removed (owing to friction) are identified.

Experimentally, this is achieved by performing a baroclinic geostrophic adjustment within a circular basin (see figure 1) that generates a geostrophic mean flow as well as baroclinic basin-scale waves (Wake *et al.* 2004*b*). Using the experimental configuration presented in figure 1, Wake *et al.* (2004*b*) identified two dimensionless parameters that may be important in characterizing the temporal evolution of the baroclinic basin-scale waves. The first parameter provides a measure of the initial forcing given by

$$\epsilon = \frac{\Delta H}{H_1} \tag{1.1}$$

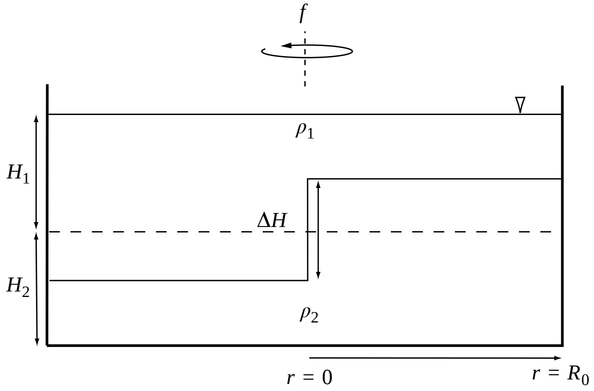

FIGURE 1. A side view of the initial condition for a baroclinic geostrophic adjustment in a circular basin of radius R_0. The step height discontinuity ΔH across the tank diameter ensures that the upper (H_1) and lower (H_2) layer depths are equally displaced from the undisturbed position of the density interface.

where ΔH is the initial step discontinuity across the basin diameter and H_1 is the undisturbed upper-layer depth (figure 1). The studies of Wake *et al.* (2004*b*) and Wake *et al.* (2004*a*) focused on the geostrophic component of the response, demonstrating that for a strong initial forcing (large ϵ) nonlinear effects result in a departure from geostrophic equilibrium after $\tau > 2\epsilon^{-1}$ (τ is time scaled by the inertial period $T_I = 2\pi/f$) while for a weak initial forcing (small ϵ), nonlinear effects are precluded by the influence of friction due to Ekman damping in the lower layer of the circular basin (see figure 1).

The second parameter is the Burger number, which provides a measure of the relative importance of stratification versus rotation, given by

$$S = \frac{R}{R_0}, \tag{1.2}$$

where R_0 is the radius of the basin, R is the baroclinic Rossby radius of deformation given by $R = c_0/f$, $c_0 = (g' H_1 H_2/(H_1 + H_2))^{1/2}$ is the linear baroclinic phase speed and f is the inertial frequency. The partitioning of energy between the geostrophic and periodic components (Stocker & Imberger 2003; Wake *et al.* 2004*b*), as well as the ratio of kinetic to potential energy contained in the baroclinic basin-scale waves (Antenucci & Imberger 2001), is dependent upon S.

Initially, experiments are performed in a circular basin with a flat bottom and vertical sidewalls in order to evaluate the influence of friction on the baroclinic basin-scale waves as well as the potential nonlinear processes that may occur during the propagation of the waves (figure 2*a*). Selected experiments are then repeated in the presence of simple topographic features, a radially protruding cape (figure2*b*(i)) and a bathymetric ridge (figure 2*b*(ii)). The bathymetric ridge introduces a third dimensionless parameter given by

$$\gamma = \frac{H_2}{H_b}, \tag{1.3}$$

where H_2 is the undisturbed lower-layer depth (figure 1) and H_b is the height of the bathymetric ridge.

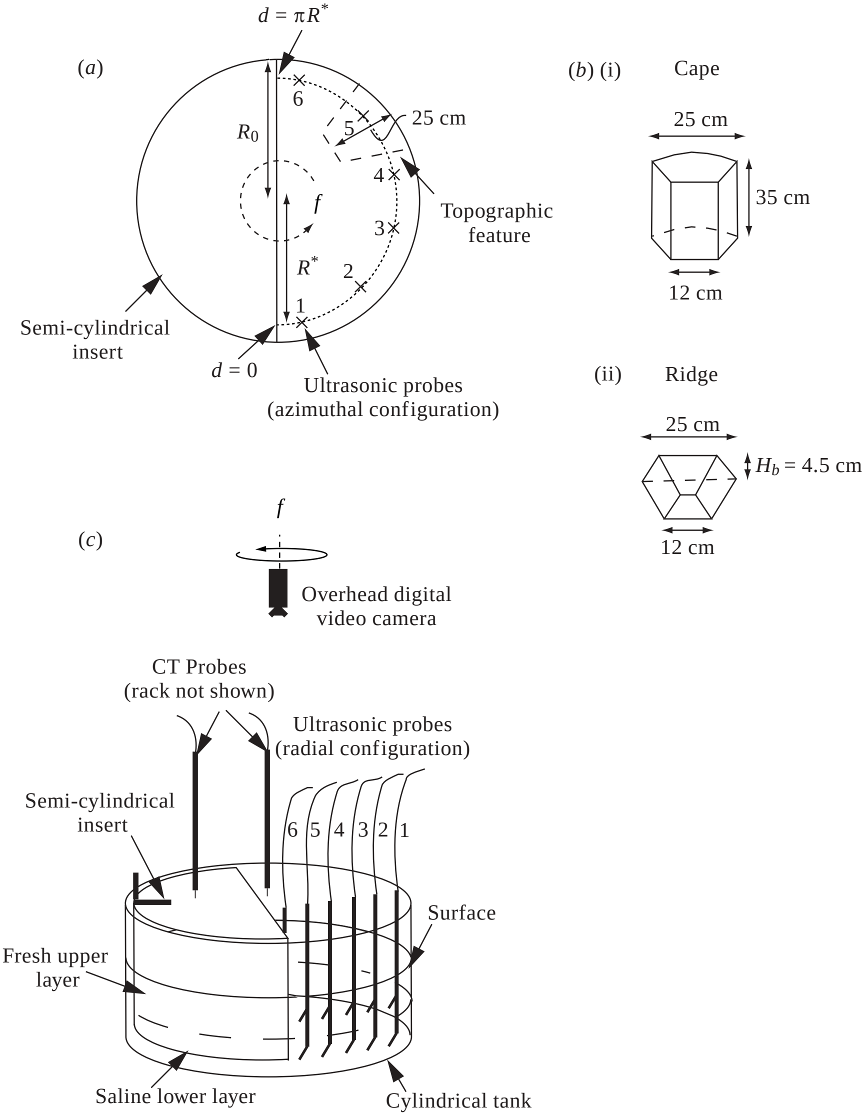

FIGURE 2. (*a*) Plan view of the experimental facility showing the azimuthal configuration of the ultrasonic probes. The probes are positioned along a radius $R^* = 41.5$ cm from the tank centre and are labelled from the semi-cylindrical insert in a cyclonic direction with positions 1–6 being 5, 30, 56, 69, 99 and 125 cm along the circumference of the semi-circle πR^*. The location and shape of the topographic feature is indicated by the region enclosed by the dashed lines. (*b*) Side view of the topographic features illustrating the azimuthal and vertical dimensions of (i) the cape and (ii) the bathymetric ridge. (*c*) Side view of the experimental facility showing the position of the two conductivity–temperature (CT) probes, the overhead digital video camera and the radial configuration of the ultrasonic probes. The distances from the sidewall to positions 1–6 are 3, 13, 20, 27, 38 and 45 cm, respectively. The two-dimensional micro acoustic Doppler velocimeter (not shown) is placed adjacent to positions 1, 3 and 5 (radial configuration) in subsequent repetitions of a given experimental run.

The remainder of the paper is arranged as follows. Section 2 introduces the experimental facility. The generation and classification of baroclinic basin-scale waves is presented in § 3. In § 4, the temporal evolution of baroclinic basin-scale waves in the absence of topography is considered and the dissipation rates for the dominant modes of the response are determined. The influence of topography on the temporal evolution is investigated in § 5. Section 6 discusses the findings of the laboratory study and the results of this work are considered in terms of their implications for the baroclinic basin-scale wave energy pathways in lakes influenced by the rotation of the Earth.

2. Experimental facility

A detailed description of the experimental facility and procedure can be found in Wake *et al.* (2004*b*). For completeness, a brief outline is presented here. The model configuration and experimental set-up are detailed in figures 1 and 2. The experiments were conducted in a 95 cm diameter cylindrical Perspex tank of depth 50 cm. The tank was mounted on a rotating turntable that revolved counterclockwise at a constant rate $\Omega = f/2$. The tank could be divided into two regions of equal volume by a removable semi-cylindrical Perspex insert (open at the top and bottom) that could be raised or lowered by means of a pulley system attached to the rotating table-top frame.

In a typical experiment, the tank containing a fresh upper layer and a saline lower layer was allowed to spin up into solid-body rotation. The semi-cylindrical insert was then carefully lowered into the tank, below the density interface, effectively partitioning the cylindrical tank into two regions: inside the semi-cylindrical insert (inner region) and outside the semi-cylindrical insert (outer region). The initial potential energy gradient and potential vorticity contrast between inner and outer regions was created by pumping fluid from the upper layer in the outer region into the upper layer of the inner region which, in turn, drove a return flow of lower-layer fluid underneath the insert. Density profiles were measured in both the inner and outer regions, in order to determine the introduced step height discontinuity, by traversing two conductivity-temperature (CT) probes over the total fluid depth once the two-layer fluid had returned to its quiescent state.

An experiment was initiated by swiftly removing the semi-cylindrical insert, using the pulley system, while at the same time ensuring that the rotation rate remained constant. The vertical interface displacements created by the release were sampled at 5 Hz from six ultrasonic probes. Experiments performed without topographic features were repeated with the probes configured azimuthally (azimuthal configuration) (figure 2*a*) and radially (radial configuration) (figure 2*c*) in order to obtain point measurements of the spatial structure and direction of propagation of the excited basin-scale waves. Time series of the radial and azimuthal velocities at mid-depth in the upper layer were collected at 10 Hz using a two-dimensional micro acoustic Doppler velocimeter (ADV). For each experiment in which the probes were in the radial configuration, the sample volume of the micro ADV was positioned adjacent to probes in positions 1, 3 and 5 in subsequent runs (figure 2*c*).

For the experimental runs that included one of the topographic features, the probes were in the radial configuration and the feature was placed in the tank prior to the addition of the fluid layers. The location of the topographic feature is illustrated in figure 2(*a*). The cape and the bathymetric ridge were designed so that their horizontal dimensions were identical (see figure 2*a*, *b*). Visualization experiments were performed for runs that included topography with dye being injected near the feature in the upper layer (cape) or lower layer (ridge) and an overhead digital video camera mounted on

Run	ΔH	H_1	H_2	g'	f	H_1/H_2	S	ϵ	Topography	γ
1	2	10	10	18.8	0.19	1	1	0.2	–	–
2	4	10	10	18.8	0.19	1	1	0.4	–	–
3	8	10	10	18.8	0.19	1	1	0.8	–	–
4	2	10	10	17.1	0.25	1	0.75	0.2	–	–
5	4	10	10	17.1	0.25	1	0.75	0.4	–	–
6	8	10	10	17.1	0.25	1	0.75	0.8	–	–
7	2	10	10	12.1	0.32	1	0.5	0.2	–	–
8	4	10	10	12.1	0.32	1	0.5	0.4	–	–
9	8	10	10	12.1	0.32	1	0.5	0.8	–	–
10	1	10	10	6.3	0.44	1	0.25	0.1	–	–
11	2	10	10	6.3	0.44	1	0.25	0.2	–	–
12	4	10	10	6.3	0.44	1	0.25	0.4	–	–
13	8	10	10	6.3	0.44	1	0.25	0.8	–	–
14	3	7.5	12.5	12.1	0.32	3/5	0.5	0.4	–	–
15	2	5	15	12.1	0.32	1/3	0.5	0.4	–	–
16	4	10	10	18.8	0.19	1	1	0.4	Cape	–
17	4	10	10	12.1	0.32	1	0.5	0.4	Cape	–
18	4	10	10	6.3	0.44	1	0.25	0.4	Cape	–
19	4	10	10	18.8	0.19	1	1	0.4	Ridge	2.2
20	3	12.5	7.5	18.8	0.19	5/3	1	0.4	Ridge	1.7
21	2	15	5	18.8	0.19	3	1	0.4	Ridge	1.1
22	4	10	10	12.1	0.32	1	0.5	0.4	Ridge	2.2
23	3	12.5	7.5	12.1	0.32	5/3	0.5	0.4	Ridge	1.7
24	2	15	5	12.1	0.32	3	0.5	0.4	Ridge	1.1
25	4	10	10	6.3	0.44	1	0.25	0.4	Ridge	2.2
26	3	12.5	7.5	6.3	0.44	5/3	0.25	0.4	Ridge	1.7
27	2	15	5	6.3	0.44	3	0.25	0.4	Ridge	1.1

TABLE 1. The experimental programme: all data in c.g.s. units.

the rotating turntable (figure 2*c*) recorded the dye movement following the initiation of an experiment.

The interface displacement η^* initially had a step height discontinuity across the tank diameter of magnitude ΔH (figure 1). The upper and lower undisturbed layer depths were H_1 and H_2, respectively. The reduced gravity g' was varied between 6.3 and 18.8 cm s^{-2} where $g' = g\Delta\rho/\rho_2$ and $\Delta\rho = \rho_2 - \rho_1$ is the density difference between the upper and lower layers and g is the acceleration due to gravity. The radius of the semi-cylindrical forcing mechanism r_f was equal to the dimensional radius R_0 of the cylindrical tank, as shown in figure 1, which was scaled with the baroclinic Rossby radius of deformation given by $R = c_0/f$ to give the Burger number $S = R/R_0$. The inertial frequency f range was 0.19–0.44 s^{-1} so that S varied between 1 and 0.25. The initial step discontinuity ΔH, was scaled by the undisturbed upper-layer depth H_1 so that $\epsilon = \Delta H/H_1$ while the interface displacement η^* was non-dimensionalized by ΔH. The initial forcing amplitude ϵ was varied between 0.1 and 0.8, while the ratio of the layer depths H_1/H_2 was varied between 1/3 and 3. The height of the bathymetric ridge H_b was scaled with the lower-layer depth H_2 and was varied between 1.1 and 2.2. Time t was scaled using the inertial period $T_I = 2\pi/f$ so that $\tau = t/T_I$ was dimensionless time, while the velocity was scaled using $\epsilon f R$ so that the dimensionless azimuthal velocity in the upper layer was $\bar{u}_a$. A summary of the experimental programme is given in table 1.

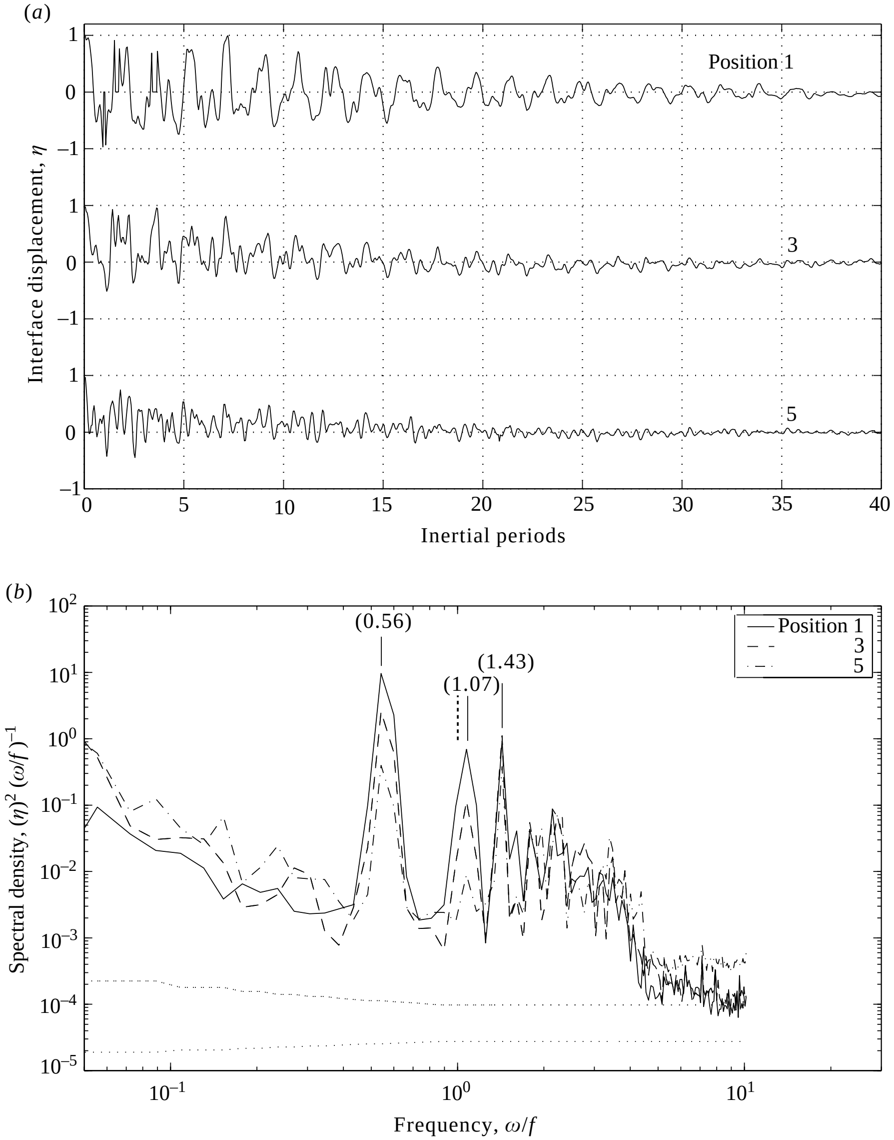

FIGURE 3. (*a*) Time series of the interface displacement η collected at 5 Hz from positions 1, 3 and 5 (radial configuration) for run 8 ($S = 0.5$, $\epsilon = 0.4$). (*b*) Power spectra of the interface displacements shown in (*a*). The wave frequency ω is scaled by f, with the dashed vertical line identifying the inertial frequency f while the solid vertical lines identify the significant peaks. Spectra have been smoothed in the frequency domain to improve confidence, with the 95% confidence level shown by the dotted lines.

3. Baroclinic basin-scale wave classification in a rotating circular basin

Initiating an experiment produces a basin-scale geostrophic flow as well as baroclinic waves. A detailed discussion of the adjustment process can be found in Wake *et al.* (2004*b*). Interface displacement and azimuthal velocity time series measured by the instrumentation in a radial configuration are presented in figures 3(*a*) and 4(*a*) for a typical run (run 8 ($S = 0.5$, $\epsilon = 0.4$)) of the experimental programme. As seen in figures 3(*a*) and 4(*a*), the response to the initial forcing is complex, consisting of

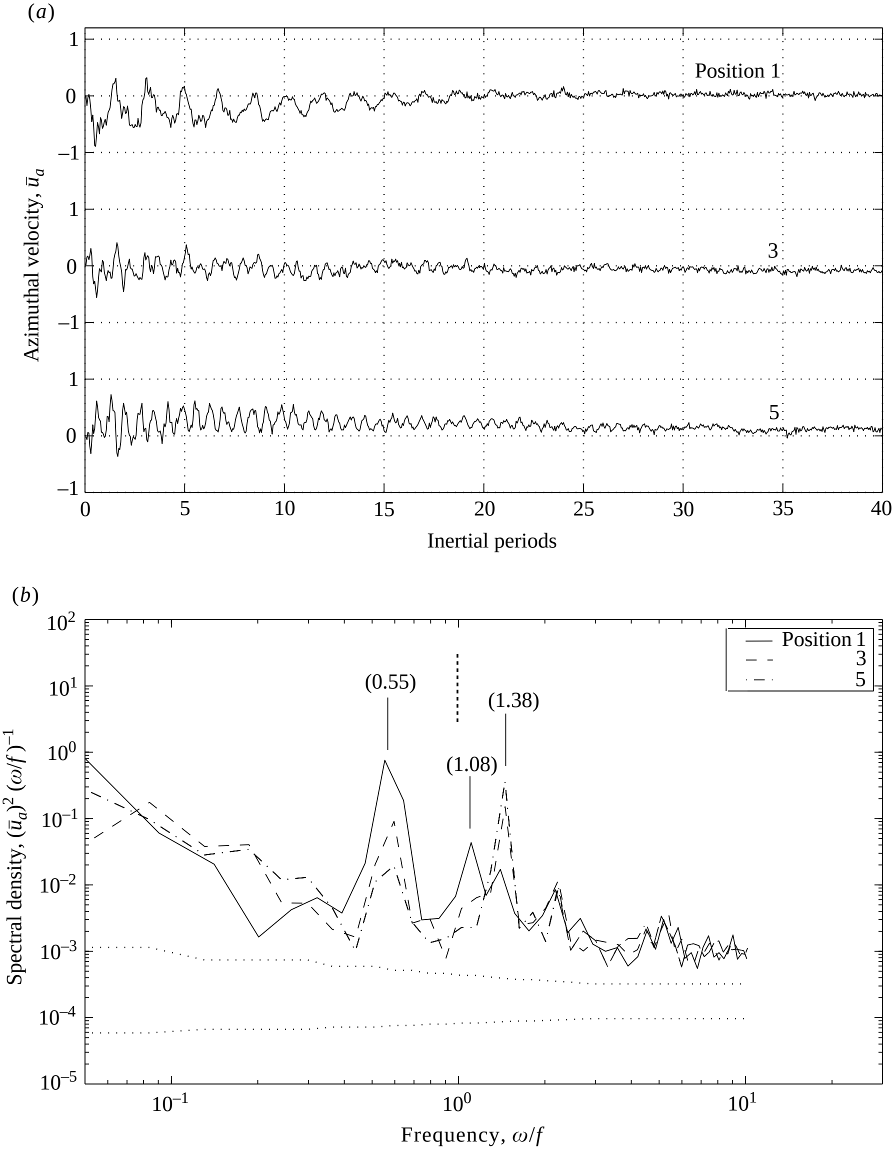

FIGURE 4. (*a*) Time series of the azimuthal velocity $\bar{u}_a$ collected at 10 Hz from positions 1, 3 and 5 (radial configuration) for run 8 ($S = 0.5$, $\epsilon = 0.4$). (*b*) Power spectra of the azimuthal velocity shown in (*a*). Spectra are smoothed in a similar manner to figure 3 (*b*).

multiple frequencies which decay in time with no wave motion evident after 40 T_I. Comparison of time series between positions 1 and 5 clearly shows that the interface displacement amplitude decays offshore. Note also that the phase between the interface displacement and velocity changes with time.

Power spectra of the interface displacement and velocity time series in figures 3(*a*) and 4(*a*) are shown in figures 3(*b*) and 4(*b*), respectively. Wave identification is on the basis that a wave of significance will exhibit spectral peaks in both displacement (figure 3*b*) and velocity (figure 4*b*) at the same frequency. Using this criterion, three

Observed	Predicted	Mode (radial, azimuthal)	Direction of propagation
0.55	0.65	(1,1)	Cyclonic
1.40	1.51	(1,1)	Anticyclonic

TABLE 2. Observed versus predicted wave frequencies ($|\omega/f|$) from (3.1) (Csanady 1967) for the dominant waves excited in run 8 ($S = 0.5$, $\epsilon = 0.4$).

S	Mode	Frequency	Type
1	$-(1,1)$	Super-inertial	Poincaré
	$+(1,1)$	Super-inertial	Poincaré
0.75	$-(1,1)$	Sub-inertial	Kelvin
	$+(1,1)$	Super-inertial	Poincaré
0.5	$-(1,1)$	Sub-inertial	Kelvin
	$-(2,1)$	Super-inertial	Kelvin
	$+(1,1)$	Super-inertial	Poincaré
0.25	$-(1,1)$	Sub-inertial	Kelvin
	$-(2,1)$	Sub-inertial	Kelvin
	$-(3,1)$	Sub-inertial	Kelvin
	$+(1,1)$	Super-inertial	Poincaré

TABLE 3. The baroclinic basin-scale waves observed in the laboratory experiments in the absence of topography. The excited modes are independent of the initial forcing, ϵ.

waves of significance can be identified for this run: a sub-inertial and two super-inertial waves.

The two dominant basin-scale waves illustrated in figures 3(*b*) and 4(*b*) have dimensionless frequencies ω/f of approximately 0.55 and 1.40, respectively. Csanady (1967) calculated the natural frequencies using the dispersion relation for super-inertial waves

$$\frac{1}{S}\sqrt{(\omega/f)^2-1}\,J_{n-1}\left(\frac{1}{S}\sqrt{(\omega/f)^2-1}\right)+n\left(\frac{1}{\omega/f}-1\right)J_n\left(\frac{1}{S}\sqrt{(\omega/f)^2-1}\right)=0, \tag{3.1}$$

where J_n is the ordinary Bessel function of order n, where n is the azimuthal mode number. Equation (3.1) is an eigenvalue problem for which solutions of increasing ω/f correspond to higher radial modes for fixed n (e.g. Antenucci & Imberger 2001). A frequency equation of identical form to (3.1) is obtained for sub-inertial waves using the identity $J_n(ix) = i^n I_n(x)$ after noting that the coefficient of the first term and the argument of the Bessel function in (3.1) is imaginary for a sub-inertial wave (Csanady 1967). Comparing the observed and predicted frequencies (see table 2) suggests that the sub-inertial wave may be classified as a cyclonically propagating azimuthal mode one, radial mode one ($-(1,1)$) wave, commonly referred to in the literature as a Kelvin wave (e.g. Csanady 1967; Antenucci & Imberger 2001). The super-inertial wave may be classified as either an anticyclonically propagating, azimuthal mode one, radial mode one ($+(1,1)$) wave or as a Poincaré wave (e.g. Csanady 1967; Antenucci & Imberger 2001). Rather than referring to the periodic response as consisting of Kelvin and Poincaré waves, which is common practice in the literature, we adopt the formal

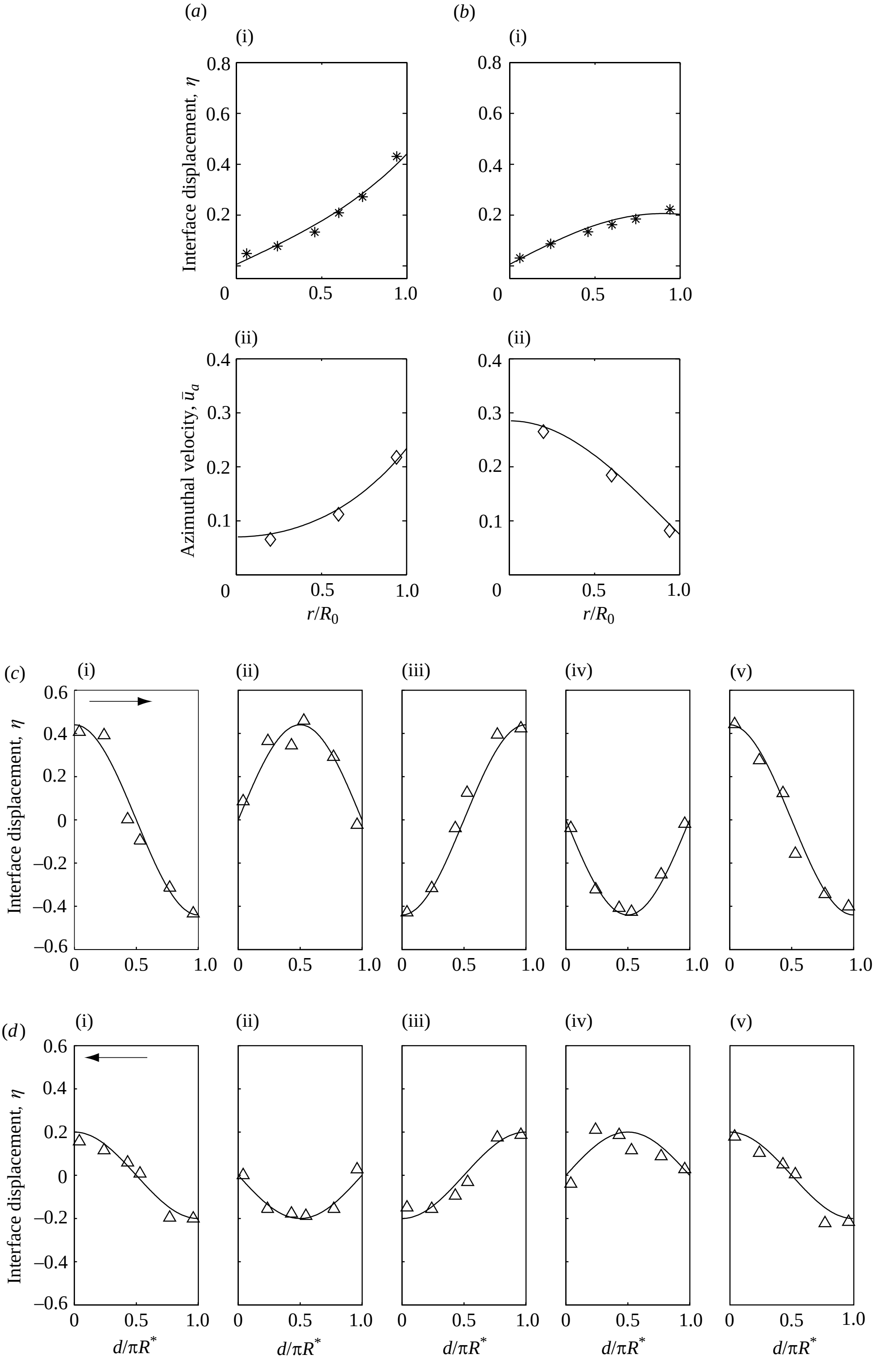

FIGURE 5. For caption see facing page.

classification because it provides an unambiguous description of the spatial structure and the direction of propagation of the wave.

Csanady (1967) used linear inviscid theory to determine the modal structure of the natural baroclinic basin-scale waves in a rotating circular basin with the interface displacement given as

$$\eta(r,\theta) = A\varphi G(r)\cos(n\theta), \tag{3.2}$$

where

$$G(r) = \begin{cases} J_n(r/R_*), & |\omega/f| > 1, \\ I_n(r/R_*), & |\omega/f| < 1, \end{cases} \tag{3.3}$$

and

$$R_* = \frac{c_0}{\sqrt{|\omega^2 - f^2|}}, \tag{3.4}$$

while the azimuthal $\bar{u}_a$ velocity in the upper layer is

$$\bar{u}_a(r,\theta) = A\frac{-\chi c_0}{\omega^2 - f^2}\left(f\frac{\mathrm{d}G}{\mathrm{d}r} + \frac{\omega n}{r}G\right)\cos(n\theta), \tag{3.5}$$

where φ and χ are coefficients associated with the transform from modal variables into layer variables and A is an unknown scaling parameter that provides the wave amplitude.

Bandpass filtering the interface displacement and azimuthal velocity time series at each measurement location (see figure 2) provides point measurements of $\eta(r,\theta)$ and $\bar{u}_a(r,\theta)$ for a given periodic mode as a function of time. Assuming that the modal structure of the wave is described by linear theory, the unknown scaling parameter A is calculated for a given instant in time as the mean of the estimates of this parameter determined at each measurement location using (3.2)–(3.5).

Consider the observed and fitted analytical predictions of the sub-inertial wave radial profile (figure 5*a*). It is evident that the observed interface displacement and velocity profiles are described well by the radial mode one profile. Similarly, for the super-inertial wave, the observed profiles agree strongly with the radial mode one profile (figure 5*b*). Now consider the observed and fitted analytical azimuthal profile for the sub-inertial (figure 5*c*) and super-inertial wave (figure 5*d*) over one wave period. In both instances, the observed azimuthal profiles are described well by the azimuthal mode one profile. Furthermore, it is clear from figures 5(*c*) and 5(*d*) that the direction of wave propagation observed in run 8 agrees with the prediction obtained from the frequency comparison with the sub-inertial wave propagating cyclonically around the basin while the super-inertial wave propagates anticyclonically.

Using this approach, all the waves identified from the experimental program are classified in table 3. Note that the excited modes are independent of ϵ and that wave classification using Kelvin/Poincaré nomenclature is also provided. The dominant

FIGURE 5. The measured and fitted analytical profiles for run 8 ($S = 0.5$, $\epsilon = 0.4$). Radial profiles of (i) the interface displacement η and (ii) the azimuthal velocity $\overline{u}_a$ after 7 T_I for (*a*) the sub-inertial wave and (*b*) the super-inertial wave. Azimuthal profiles of interface displacement η over one wave period after 7 T_I for (*c*) the sub-inertial wave and (*d*) the super-inertial wave. Sequential panels illustrate the change in the azimuthal interface displacement over 1/4 of the wave period while the arrows in (*c*) (i) and (*d*) (i) indicate the direction of wave propagation. The solid line is the fitted analytical profile while the asterisks ($*$), diamonds ($\diamond$) and triangles ($\triangle$) represent the measured values. Error estimates are of the order of instrument sensitivity (± 0.02 for the ultrasonic probes and ± 0.04 for the micro ADV).

waves over the experimental regime are the −(1,1) and +(1,1) waves with the higher modes constituting a minor fraction of the periodic response ($<$ 10% of the total wave energy calculated using the method presented in §4), a result previously determined analytically (Stocker & Imberger 2003). The remainder of this study focuses on the temporal evolution of the −(1,1) and +(1,1) waves.

4. The temporal evolution of baroclinic basin-scale waves in a rotating circular basin

The temporal evolution of the dominant basin-scale waves is investigated by comparing the filtered point measurements with the fitted analytical predictions of the wave profile every time a wave crest or trough is observed in the radially configured time series measurements. Because of the end effects associated with the bandpass filtering technique, $3\,T_I$ (approximately one wave period of the gravest mode excited when $S = 0.25$) is adopted as the earliest time after which the filtered point measurements of individual waves from different experimental runs may be compared.

The temporal evolution of the radial and azimuthal profile for the −(1,1) wave and the +(1,1) wave over the first 15 T_I for run 8 is illustrated in figures 6 and 7 and clearly shows that the dominant waves are described well by linear theory although the wave amplitude decreases during this period.

Figure 8 shows the power spectra of the interface displacement and azimuthal velocity measurements taken from position 3 (radial configuration) (see figure 2*c*) for a range of the initial forcing ϵ. The amplitude of the basin-scale wave spectral peaks remain constant and the high-frequency end of the spectra remains unchanged, suggesting that varying ϵ does not change the composition of the periodic response. Using the bandpass filtering technique as before, the temporal evolution of the −(1,1) and +(1,1) waves in runs 7, 8 and 9 is determined and in all cases is described well by linear theory with the wave amplitude reducing in time.

Comparison between experimental runs for which ϵ remains constant but the influence of rotation S is varied, yields a similar result with the measured radial and azimuthal structure of the −(1,1) and +(1,1) basin-scale waves retaining a linear form until the waves are dissipated. Antenucci & Imberger (2001) derived the ratio of kinetic (KE) to potential (PE) energy as a function of S for basin-scale waves using linear theory. Given that the −(1,1) and +(1,1) waves exhibit a linear form until dissipated, the PE/KE ratios may now be used in conjunction with the fitted linear amplitudes to calculate the temporal evolution of the KE, PE and total energy of these waves. In figure 9, the energy in the −(1,1) wave, the +(1,1) wave, and the total wave energy ($TWE =$ the sum of these two components) are plotted versus the number of inertial periods. The influence of S and ϵ on the partitioning of energy between the −(1,1) wave and the +(1,1) wave as time proceeds, as well as the total wave dissipation rate, is shown. All plots have been normalized by the total wave energy after $3\,T_I$ (TWE_0). Stocker & Imberger (2003) noted that the initial partitioning of energy between the two gravest modes is a function of S. For the limited range of S considered here, the −(1,1) wave accounts for 60–65% of the total wave energy and the remaining 35–40% resides in the +(1,1) wave with the initial energy partitioning between the −(1,1) wave and the +(1,1) wave being maintained at all times. This partitioning of energy does not exhibit a noticeable dependence on ϵ, suggesting that the decay of wave energy is not associated with the nonlinear transfer of energy between the modes or to higher-frequency waves. Moreover, the steady decay of the basin-scale waves suggests that, despite the fact that the geostrophic and periodic components of the response remain trapped within the bounded domain and have

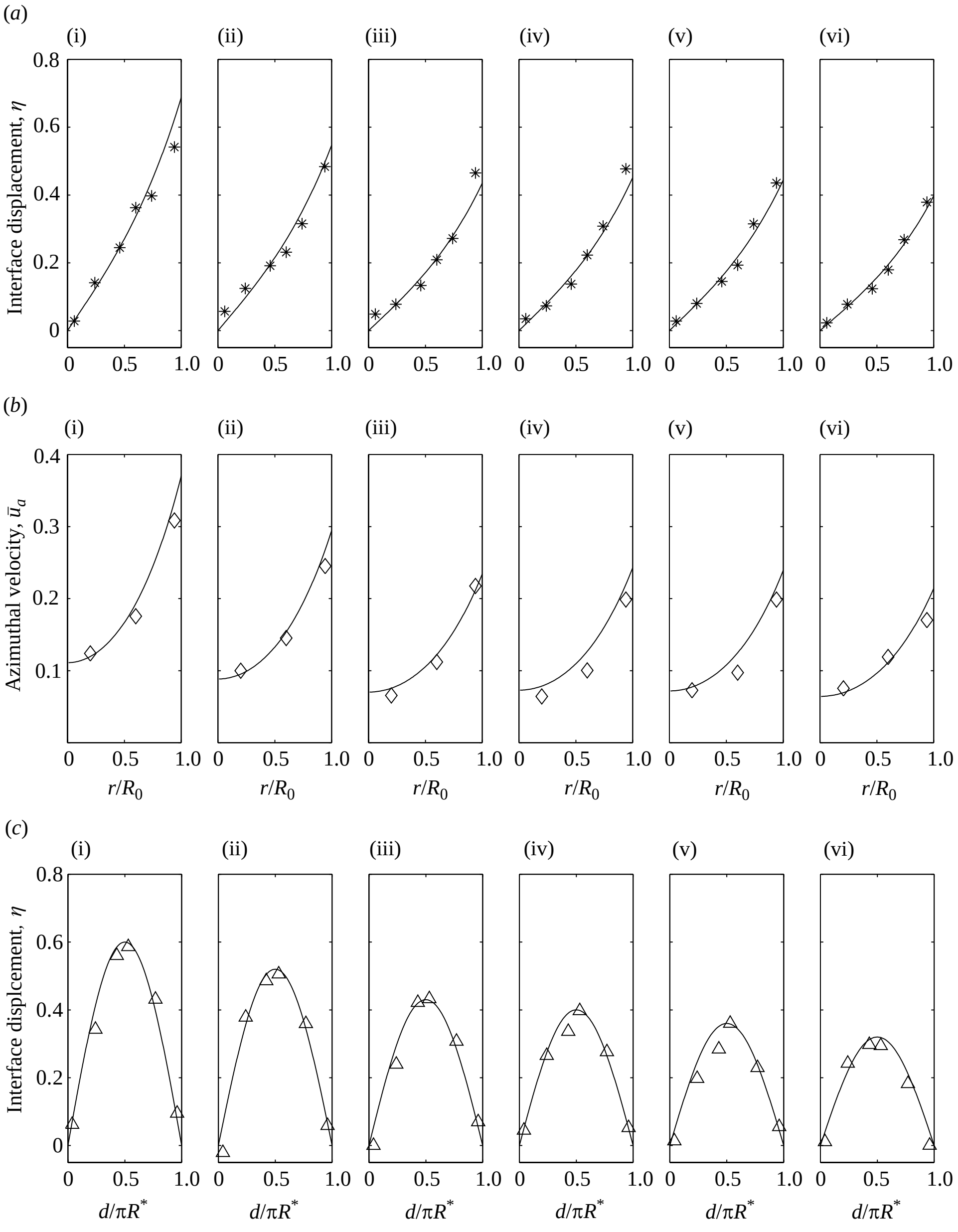

FIGURE 6. Comparison between the fitted analytical profiles and the measured (*a*) interface displacement η (radial configuration), (*b*) azimuthal velocity $\overline{u}_a$ (radial configuration) and (*c*) interface displacement η (azimuthal configuration) of the −(1,1) sub-inertial wave for run 8 ($S = 0.5, \epsilon = 0.4$) after approximately (i) 3 T_I, (ii) 5 T_I, (iii) 7 T_I, (iv) 9 T_I, (v) 11 T_I and (vi) 13 T_I. The solid lines are the fitted analytical solution while the asterisks, triangles and diamonds are the measured interface displacements (radial and azimuthal configuration) and the azimuthal velocities, respectively. Error estimates are identical to those calculated in figure 5.

comparable velocities (see figure 4*a*), there is little evidence for nonlinear wave–mean flow interaction. This observation provides experimental support for the theoretical studies of Reznik & Grimshaw (2002) and Zeitlin *et al.* (2003), which argued that the fast (wave) and slow (geostrophic flow) components of the response following a

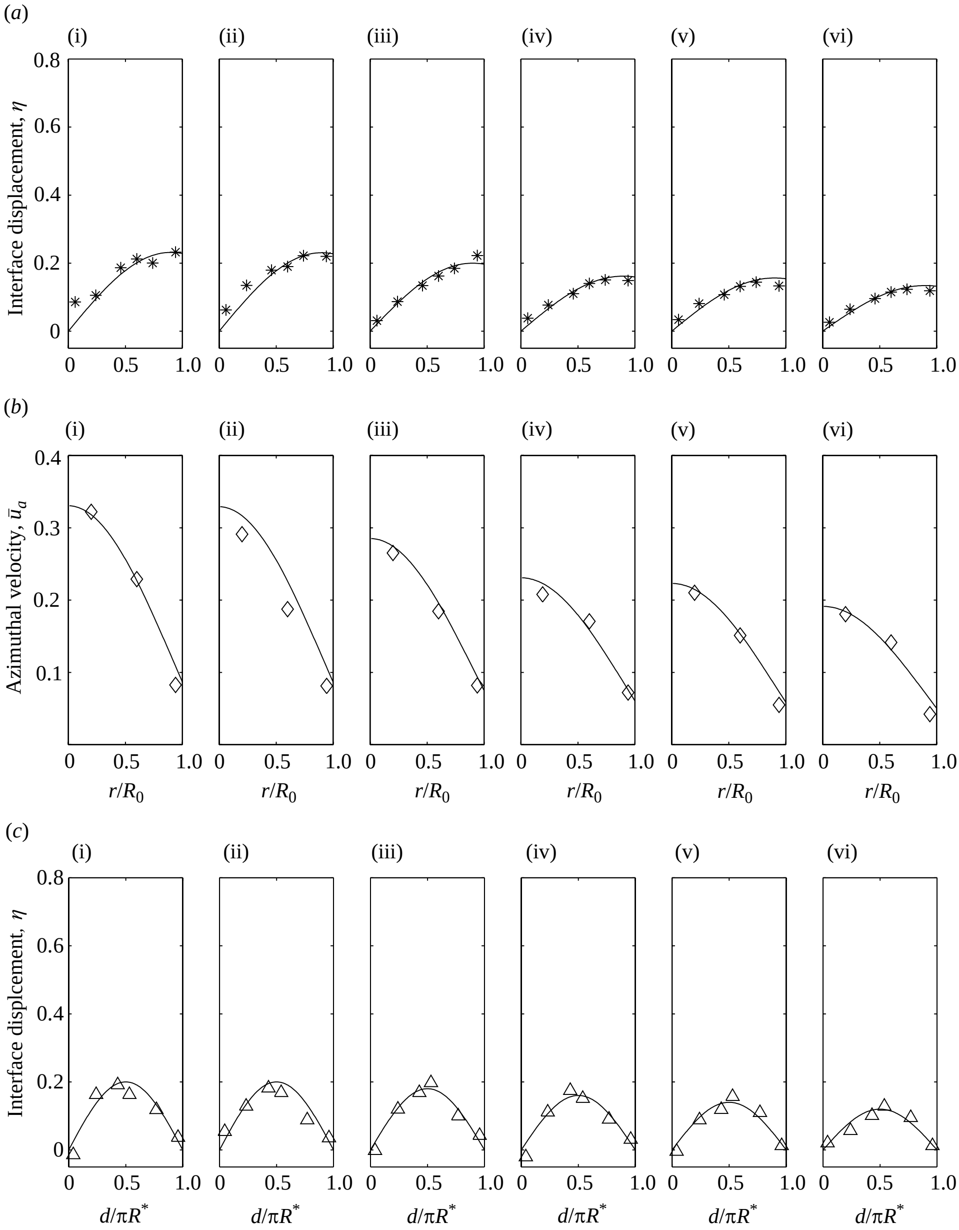

FIGURE 7. Comparison between the fitted analytical profiles and the measured (*a*) interface displacement η (radial configuration), (*b*) azimuthal velocity $\overline{u}_a$ (radial configuration) and (*c*) interface displacement η (azimuthal configuration) of the $+(1,1)$ super-inertial wave for run 8 ($S = 0.5, \epsilon = 0.4$) after approximately (i) 3 T_I, (ii) 5 T_I, (iii) 7 T_I, (iv) 9 T_I, (v) 11 T_I and (vi) 13 T_I. The solid lines are the fitted analytical solution while the asterisks, triangles and diamonds are the measured interface displacements (radial and azimuthal configuration) and the azimuthal velocities, respectively. Error estimates are identical to those calculated in figure 5.

geostrophic adjustment will not undergo a wave–mean flow interaction. The decay of wave energy is exponential in character and is independent of ϵ, but exhibits a dependence on S. Functions of the form $e^{-K\tau}$ (τ is time scaled by T_I) are fitted, using the least-squares method, to the total wave energy presented in panels (i)–(iii)

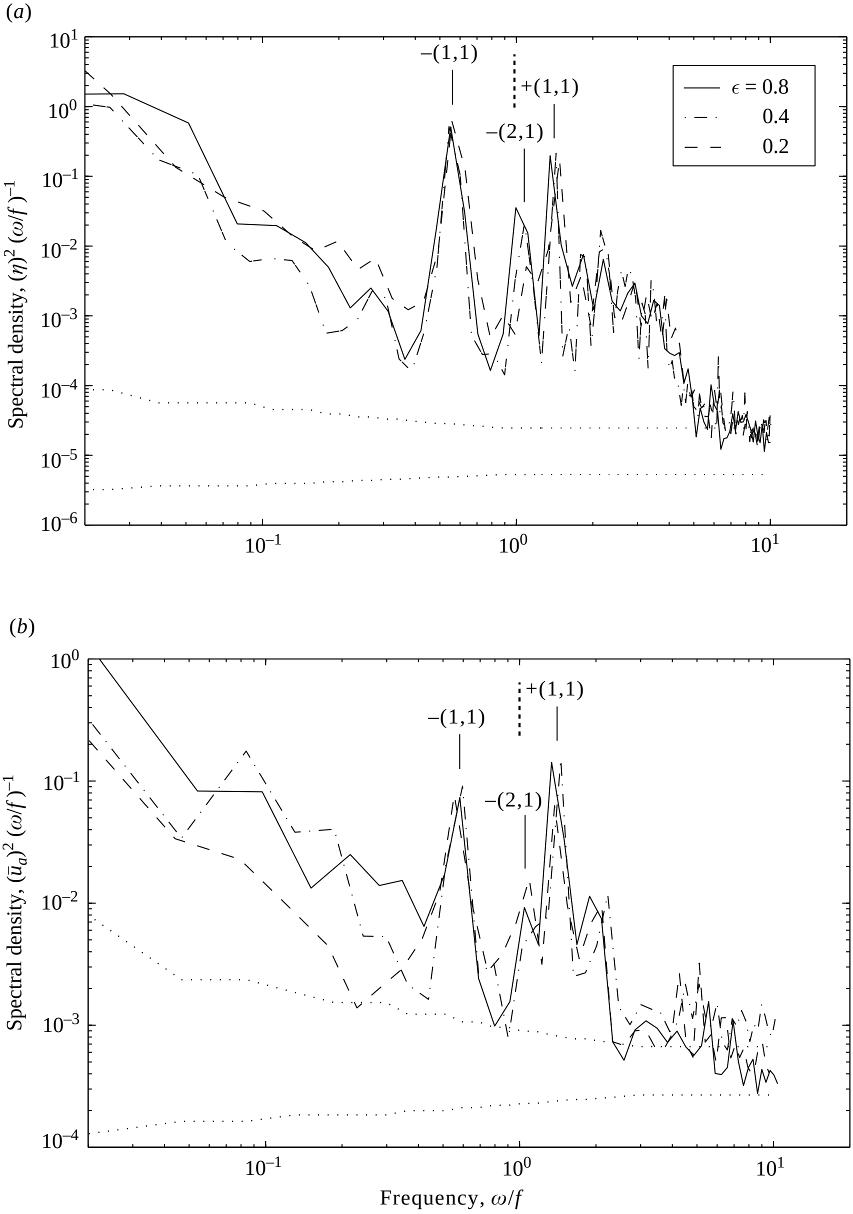

FIGURE 8. Power spectra of the (*a*) interface displacement η and (*b*) azimuthal velocity $\overline{u}_a$ measured from position 3 (radial configuration) for run 7 ($S = 0.5$, $\epsilon = 0.2$), run 8 ($S = 0.5$, $\epsilon = 0.4$) and run 9 ($S = 0.5$, $\epsilon = 0.8$). Spectra are smoothed in a similar manner to figure 3 (*b*).

of figure 9(*a*) to provide an estimate of the dimensionless decay coefficient K for the dominant waves as a function of S (see table 4).

5. Influence of topography on the temporal evolution

5.1. *Cape*

The influence of the cape on the temporal evolution of the baroclinic basin-scale waves is shown in figure 10. The power spectra of the interface displacement measured from

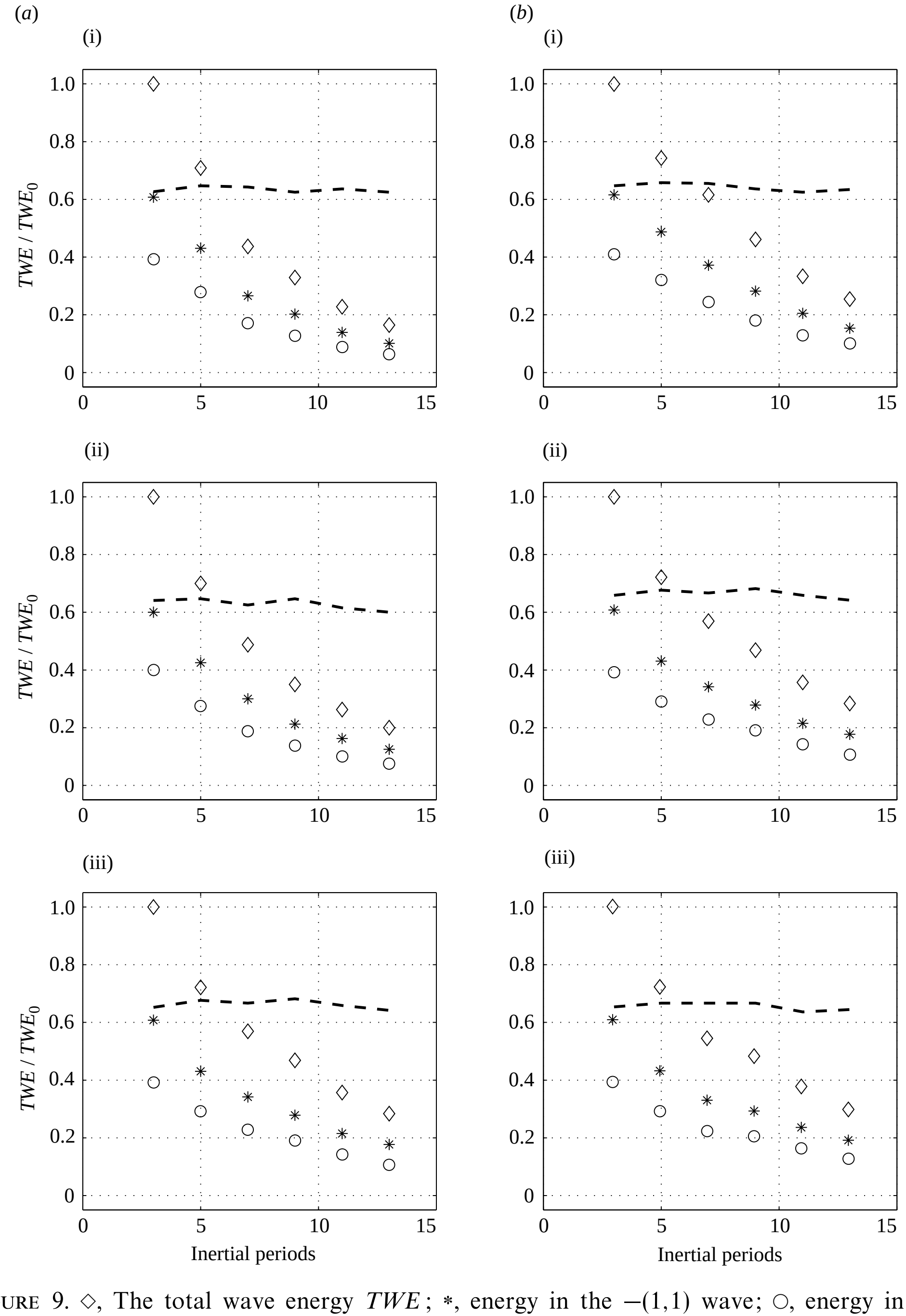

FIGURE 9. ◇, The total wave energy TWE; $*$, energy in the $-(1,1)$ wave; ○, energy in the $+(1,1)$ wave; and - - -, the energy ratio $+(1,1)/-(1,1)$ versus inertial periods (a) for a range of S (i) run 2 ($S = 1$, $\epsilon = 0.4$), (ii) run 5 ($S = 0.75$, $\epsilon = 0.4$) and (iii) run 8 ($S = 0.5$, $\epsilon = 0.4$) and (b) for a range of ϵ (i) run 7 ($S = 0.5$, $\epsilon = 0.2$), (ii) run 8 ($S = 0.5$, $\epsilon = 0.4$) and (iii) run 9 ($S = 0.5$, $\epsilon = 0.8$). Wave energy is normalized by the total wave energy after approximately 3 T_I (TWE_0).

S	K
0.5	0.07
0.75	0.09
1	0.1

TABLE 4. Decay coefficient K as a function of S, determined from the decay of total wave energy (TWE) from the dominant basin-scale waves illustrated in panels (i)–(iii) of figure 9(*a*).

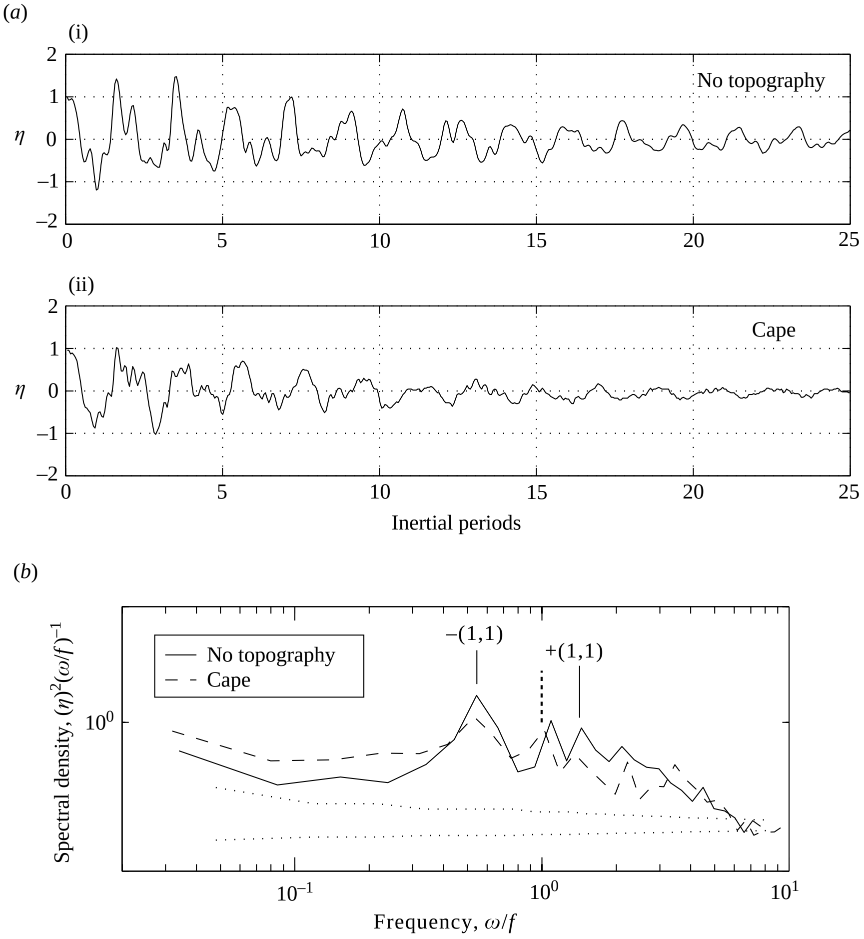

FIGURE 10. (*a*) Time series of the interface displacement η from position 1 (radial configuration) (i) with no topography (run 8 ($S = 0.5$, $\epsilon = 0.4$)) and (ii) with the cape (run 17 ($S = 0.5$, $\epsilon = 0.4$)). (*b*) Power spectra of the interface displacements shown in (*a*). Spectra are smoothed in a similar manner to figure 3 (*b*).

position 1 (radial configuration) indicate that in the presence of the cape, the spectral peak associated with the +(1,1) wave is not observed, suggesting that it is not excited as part of the periodic response. Such a result has been previously reported by Csanady (1973) who noted that this mode is not observed if the symmetry of the circular basin is sufficiently altered by topography.

The −(1,1) wave is observed, but with a reduced amplitude. The similarity between the higher-frequency end of the power spectra (frequencies greater than the frequency of the +(1,1) wave) suggests that the reduced amplitude of the −(1,1) wave, owing to the wave/topography interaction, is not a result of the transfer of energy from the basin-scale mode to higher-frequency waves. As noted by an anonymous referee, the low-frequency end of the power spectra in the presence of the cape contains more energy, suggesting that the reduced amplitude of the −(1,1) wave, owing to the wave/topography interaction, results in a transfer of energy to lower-frequency motions. Figure 11 shows the results of a dye study conducted in the upper layer with the cape in place. Figure 11(*a*) indicates the position of the dye in the upper layer prior to the removal of the semi-cylindrical insert while figures 11(*b*)–11(*f*) present the observed dye dispersion during the first three −(1,1) wave periods.

After an experiment is initiated, the leading −(1,1) wave trough encounters the cape with the dramatic variation in longshore topography resulting in flow separation and the generation of weak anticyclonic eddies at points A_1 and A_2, indicated in figure 11(*b*). As the direction of the flow reverses with the arrival of the −(1,1) wave crest at the cape, the weakly formed anticyclonic eddies are sheared apart and the reversal in flow direction results in flow separation at points C_1 and C_2 (figure 11*c*) which, in turn, generates cyclonic eddies that move into the interior of the tank. Eddy generation by this mechanism, at the expense of the −(1,1) wave, is observed over the study period (see figures 11*c*–11*f*) and is also occurring concurrently in the lower layer (not shown). The preferential formation of cyclonic eddies owing to flow separation in a wave-forced flow has previously been reported by Ivey & Maxworthy (1992). The observed lengthscale of the cyclonic eddies in both studies (the present study and that of Ivey & Maxworthy 1992) is independent of S, suggesting that the eddy injection scale is dependent upon the geometry of the cape.

5.2. *Bathymetric ridge*

Figure 12(*a*) compares measured interface displacements from position 1 (radial configuration) for γ, defined in (1.3), between 1.1 and 2.2. The decay of the periodic response is clearly a function of γ, with the rate of energy loss from the waves increasing as γ decreases. Corresponding power spectra in figure 12(*b*) indicate that the amplitude of the spectral peak due to the +(1,1) wave remains unchanged for $\gamma = 2.2$ and $\gamma = 1.7$, but is not detected when $\gamma = 1.1$. The suggestion is that when $\gamma \approx 1$, the ridge acts in an analogous fashion to the cape, sufficiently altering the symmetry of the lower layer of the circular basin so that the gravest anticyclonic mode is not excited (Csanady 1973). The amplitude of the spectral peak due to the −(1,1) wave is a function of γ, with the amplitude reducing as $\gamma \rightarrow 1$. The similarity between the higher frequency end of the power spectra plotted in figure 12(*b*) suggests that the observed increase in the decay rate of the −(1,1) wave due to the wave/topography interaction is not associated with the transfer of basin-scale wave energy to higher periodic modes.

Consider the dye study shown in figure 13 which demonstrates the dye dispersion in the lower layer owing to the presence of the bathymetric ridge in run 24 ($\gamma = 1.1$). The longshore anticyclonic flow along the sidewall boundary established in the wake of the leading trough of the −(1, 1) wave in the absence of topography (Wake *et al.* 2004*b*) is not apparent, with the dye movement being directed offshore during the first −(1,1) wave period. It is during this period that a rapid reduction in amplitude of

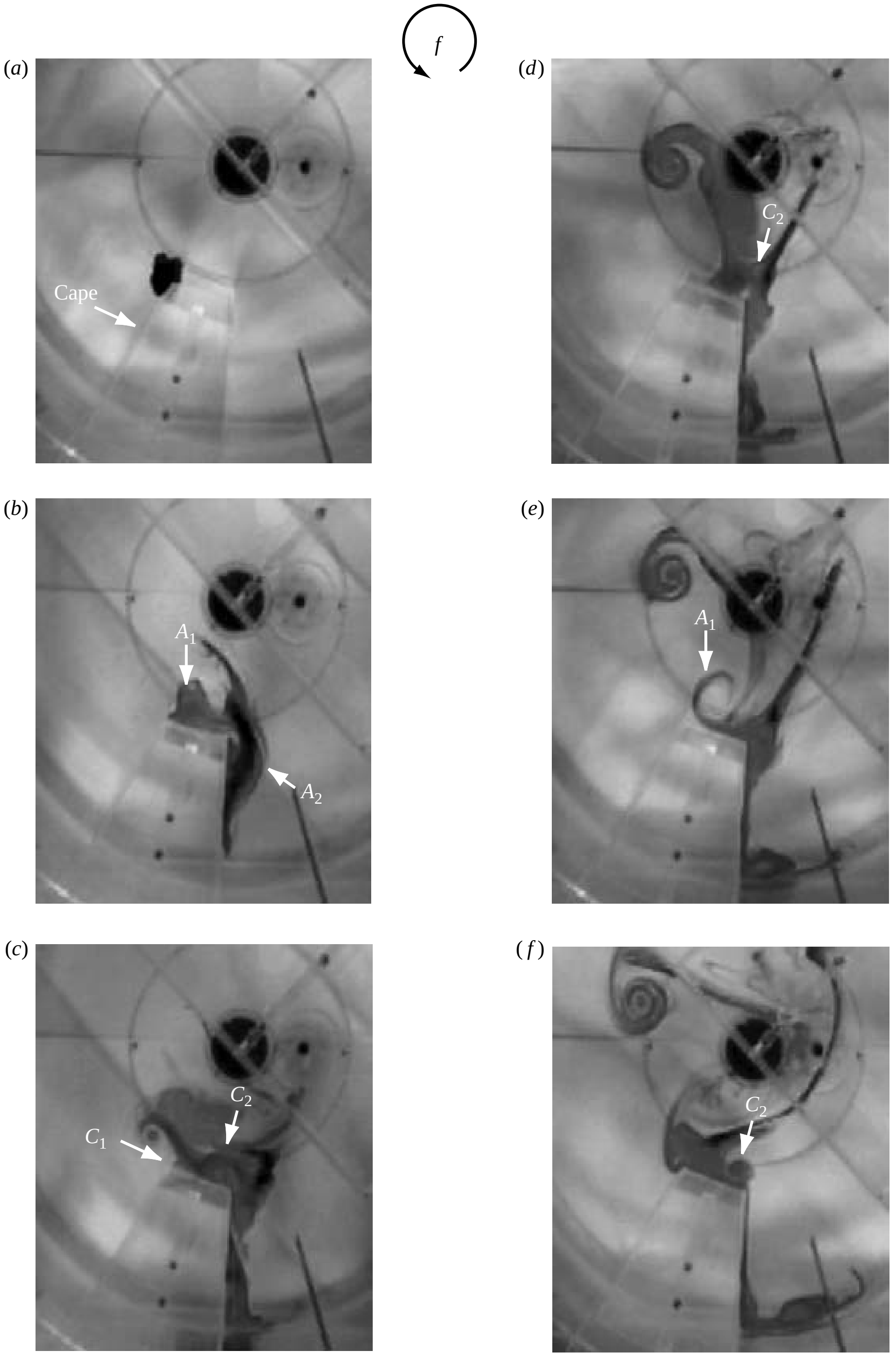

FIGURE 11. Plan view images taken from the overhead digital video camera of dye streak lines in the upper layer owing to the wave/topography interaction associated with the cape in run 17 ($S = 0.5$, $\epsilon = 0.4$). (*a*) The position of the dye prior to initiation of an experiment. (*b*) The dye dispersion after 0.5, 1, 2, 2.5 and 3 periods of the $-(1,1)$ wave, respectively. Rotation is in a counterclockwise direction.

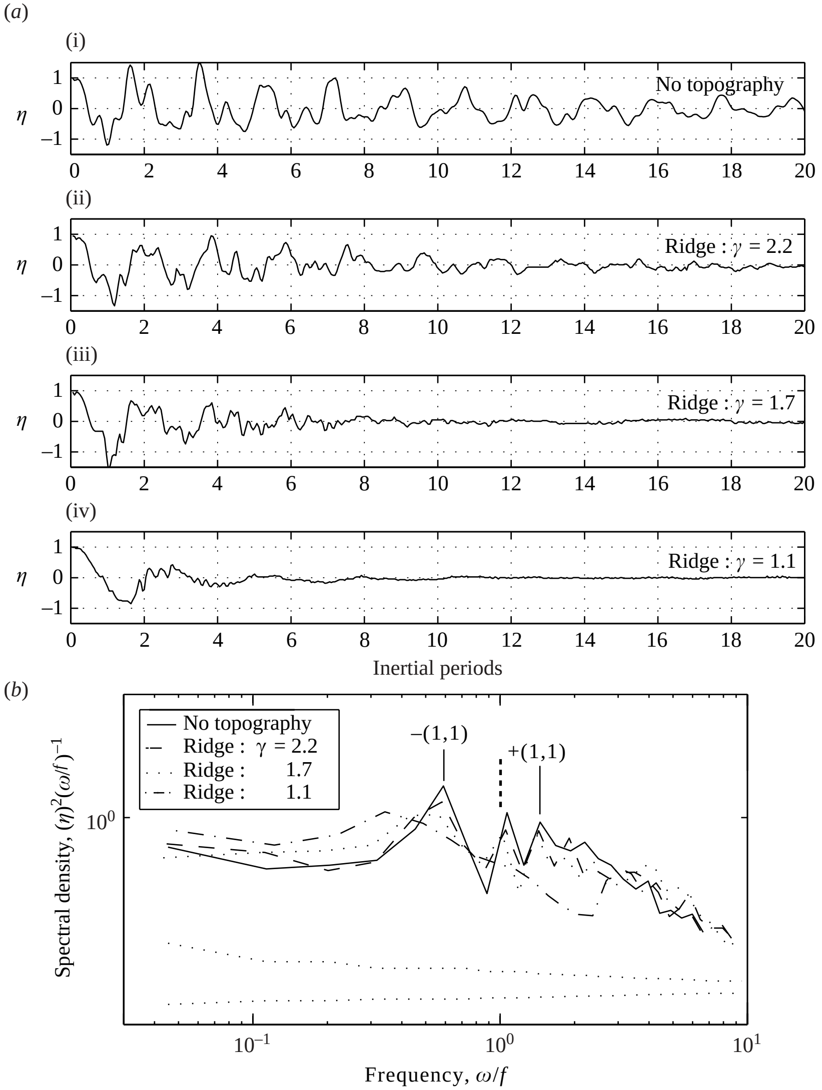

FIGURE 12. (*a*) Time series of the interface displacement η from position 1 (radial configuration) for (i) run 8 (no topography, $S=0.5$, $\epsilon=0.4$), (ii) run 22 ($\gamma=2.2$, $S=0.5$, $\epsilon=0.4$), (iii) run 23 ($\gamma=1.7$, $S=0.5$, $\epsilon=0.4$) and (iv) run 24 ($\gamma=1.1$, $S=0.5$, $\epsilon = 0.4$). (*b*) Power spectra of the interface displacements shown in (*a*). Spectra are smoothed in a similar manner to figure 3 (*b*).

the –(1,1) wave is observed (see figure 12*a*(iv)), suggesting that the wave/topography interaction generates an offshore flow at the expense of the –(1,1) wave.

For longer time, the offshore flow moves towards the interior of the basin where it interacts with the geostrophic flow established across the basin diameter by the initiation of the experiment (figure 13*d–f*) (Wake *et al.* 2004*b*).

A similar offshore flow is observed during the first –(1,1) wave period for $\gamma=1.7$ and $\gamma=2.2$. The wave/topography interaction is not as pronounced in such cases (see figure 12), so the longer time behaviour is complicated by successive wave crests and troughs of the –(1,1) wave interacting with the bathymetric ridge.

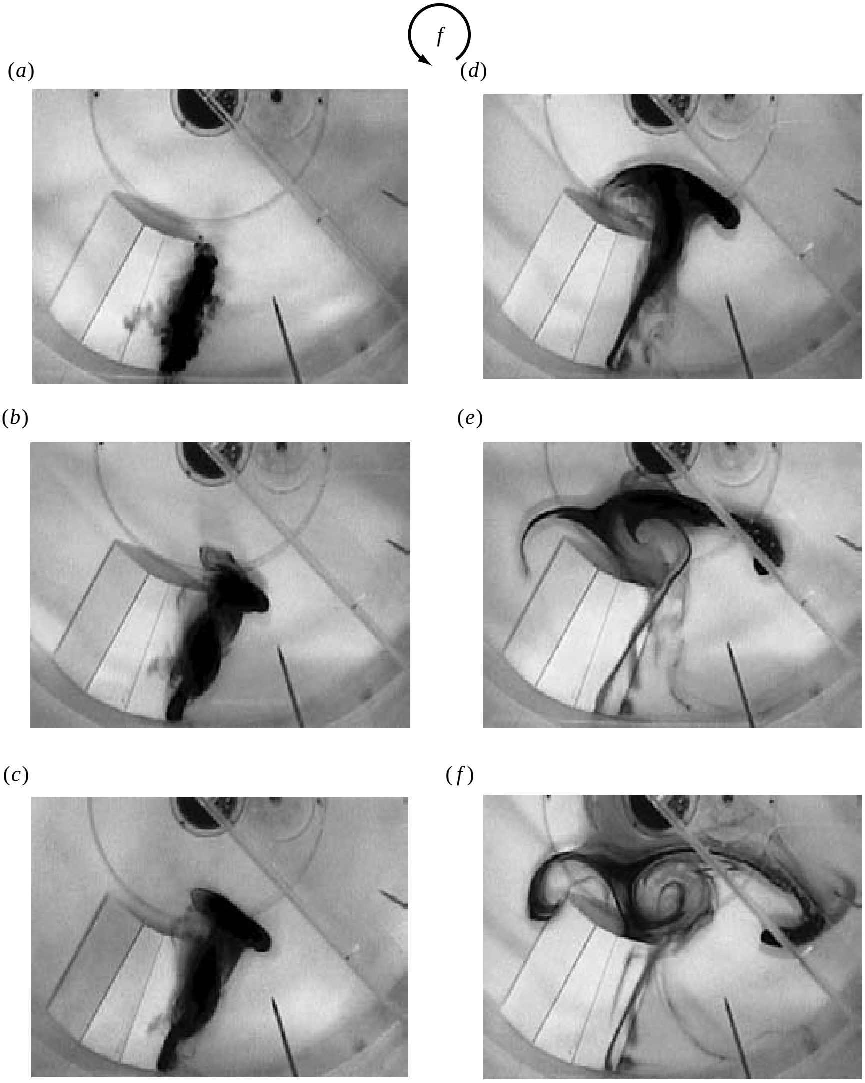

FIGURE 13. Plan view images taken from the overhead digital video camera of dye streak lines in the lower layer owing to the wave/topography interaction associated with the bathymetric ridge in run 24 ($\gamma = 1.1$, $S = 0.5$, $\epsilon = 0.4$). (*a*) The position of the dye prior to initiation of an experiment. (*b*) The dye dispersion after 0.5, 1, 2, 2.5 and 3 periods of the –(1,1) wave, respectively. Rotation is in a counterclockwise direction.

5.3. *Baroclinic basin-scale wave decay in the presence of topography*

The introduction of the cape or the bathymetric ridge into the circular basin results in interactions between the –(1,1) wave and the topography that leads to the rapid transfer of energy from the basin-scale wave to an eddy field (cape) or an offshore flow (bathymetric ridge). The techniques developed earlier may be used to compare the rate of energy loss from the –(1,1) wave, owing to the topography, with the decay rate in the absence of topography.

From figure 14, it is estimated that in the absence of topography, the –(1,1) wave loses approximately 15% of its energy over the first wave period, for example. This

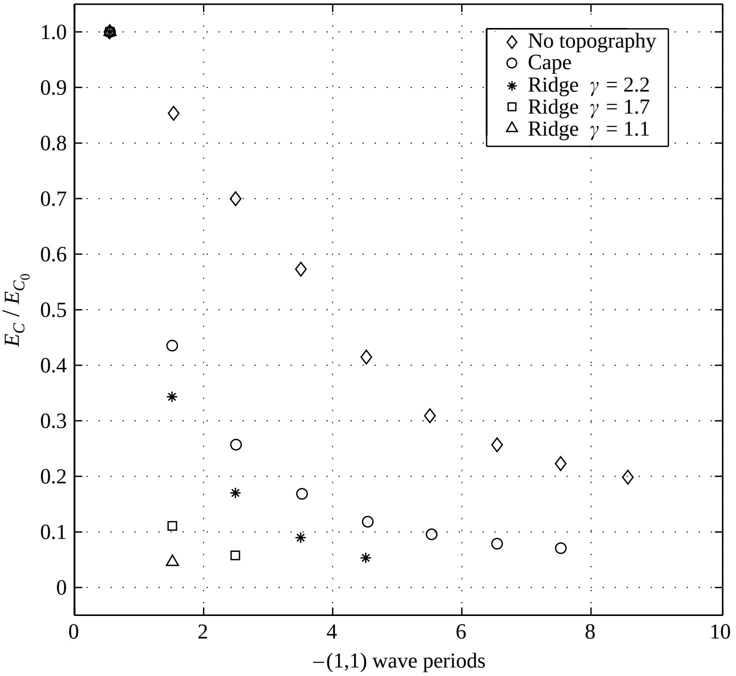

FIGURE 14. The energy in the −(1,1) wave E_C versus the −(1,1) wave period, for $S = 0.5$ and $\epsilon = 0.4$; ◇, with no topography (run 8); ○, with the cape (run 17); ∗, with the ridge where $\gamma = 2.2$ (run 22); □, $\gamma = 1.7$ (run 23); △, $\gamma = 1.1$ (run 24).

energy loss increases to about 55% with the introduction of the cape, which implies that an additional 40% of the initial energy in the −(1,1) wave is transferred during the first wave period to the eddy field generated by the wave/topography interaction. Similarly for the bathymetric ridge, the energy transferred during the first wave period is approximately 60% ($\gamma = 2.2$) and then increases with increasing height of the ridge to 75% ($\gamma = 1.7$) and 80% ($\gamma = 1.1$).

6. Discussion and conclusions

In the absence of topography, the basin-scale wave amplitude decays in time. It has been demonstrated that the nonlinear transfer of basin-scale wave energy cannot account for this observation, suggesting that wave decay is due to the influence of boundary friction. In the experiment, friction acts in a complicated fashion, with contributions from unsteady Ekman layers which form on the density interface and the tank bottom and unsteady Stewartson layers which form on the sidewall boundary of the tank in each layer after approximately one T_I (e.g. Pedlosky 1987). Previous laboratory studies on rotating flows (e.g. Condie & Ivey 1988; Jacobs & Davies 1999) have captured the influence of complex frictional mechanisms by using simple models that consider the force balance at a point in the flow, subject to steady boundary layers estimated using $\delta \sim (\nu/f)^{1/2}$. We adopt a similar approach, noting that the frictional terms can be parameterized as

$$\nu\nabla^2\boldsymbol{u} \sim \nu\frac{u}{\delta^2} \sim fu, \tag{6.1}$$

after assuming a steady boundary-layer thickness.

S	τ_K	τ_D
0.5	14	14
0.75	11	12
1	10	8

TABLE 5. Comparison between the e-folding timescale (in inertial periods) for dissipation determined from experiments for the dominant waves τ_K (see table 4) and the Ekman damping timescale τ_D (6.2).

The influence of friction can thus be included in the linearized rotating shallow-water equations using a Rayleigh friction term (Ku) where K is an effective decay coefficient. Stocker, Imberger & D'Alpaos (2000) demonstrated that in a rotating circular basin, the spatial structure of interface displacement and azimuthal velocity determined from such a set of governing equations is the same as the linear inviscid solution (3.2 and 3.5), but the wave amplitude decays exponentially in time according to $e^{-K\tau}$. Experimental observations presented in figure 9 are consistent with this simple model of frictional damping, with estimates of the dimensionless decay coefficient K for the dominant waves over a range of S being provided in table 4.

The characteristic e-folding time scale due to dissipation by Ekman damping in the lower layer (e.g. Gill 1982) after scaling with T_I, is given by

$$\tau_D = \frac{H_2}{\pi}\left(\frac{f}{2\nu}\right)^{1/2}, \tag{6.2}$$

and can be estimated for the experiments using the parameters given in table 1. The predictions from 6.2 and those obtained from the experimentally observed decay coefficients are shown in table 5, and the good agreement implies that, despite the complicated frictional influence in operation, wave dissipation can be modelled using steady Ekman dynamics associated with the tank bottom in the lower layer.

The introduction of topographic features significantly changes the composition of the periodic response (the +(1,1) wave was no longer observed) as well as decay rate of the –(1,1) wave owing to wave/topography interactions. For the –(1,1) wave to be significantly affected by the cape, the variation in the offshore length scale of the topography L_R, must be large in comparison to the characteristic radial length scale R of the –(1,1) wave. This occurs when

$$S_R = \frac{R}{L_R} < O(1). \tag{6.3}$$

Now consider the interaction between the –(1,1) wave and the bathymetric ridge. Note that the offshore flow generated by this interaction is evident after half a wave period (see figure 13*b*) which suggests that its generation is associated with the propagation of the leading –(1,1) wave trough over the ridge. The bathymetric ridge partitions the lower layer into three regions: region 1 is downstream of the ridge, region 2 is above the ridge, and region 3 is upstream of the ridge. Ignoring frictional effects, then conserving potential vorticity before and after the wave of depression has passed region 1, yields

$$\zeta_1 = -\frac{f\eta}{H_2}, \tag{6.4}$$

where ζ_1 is the anticyclonic relative vorticity of a fluid column in region 1 induced by the passage of the wave of depression. Similarly, for region 2

$$\zeta_2 = -\frac{f\eta}{H_2 - H_b}. \tag{6.5}$$

Combining (6.4) and (6.5), and using $\gamma = H_2/H_b$ gives

$$\zeta_2 = \frac{\gamma}{\gamma - 1}\zeta_1. \tag{6.6}$$

Defining $\zeta_{bd} = \zeta_2 - \zeta_1$ and using (6.6) yields

$$\zeta_{bd} = \frac{1}{\gamma - 1}\zeta_1, \tag{6.7}$$

so that the relative vorticity introduced over the downstream face ζ_{bd} is anticyclonic. Using a similar argument to the one given above,

$$\zeta_{bu} = -\frac{1}{\gamma - 1}\zeta_1, \tag{6.8}$$

so that the relative vorticity introduced over the upstream face of the bathymetric ridge ζ_{bu} is cyclonic.

In the absence of the bathymetric ridge, the –(1,1) wave trough compresses fluid columns in the lower layer, generating an anticyclonic boundary current in its wake (Wake *et al.* 2004*b*). For the –(1,1) wave trough to interact with the ridge, the time scale for fluid columns to acquire relative vorticity ($T_I \sim 1/f$), owing to compression/stretching of fluid columns as they move over the topography, must be less than the advection time scale over the ridge given by $T_{AD} = L_\theta/u_b$, where L_θ is the azimuthal length scale of the ridge and $u_b \sim \epsilon c_0$ is the characteristic velocity of the anticyclonic boundary current (Wake *et al.* 2004*b*). This condition can be expressed as

$$\frac{1}{f} < \frac{L_\theta}{\epsilon c_0}, \tag{6.9}$$

so that the –(1,1) wave will interact with the ridge when

$$\epsilon S_\theta < O(1), \tag{6.10}$$

where $S_\theta = R/L_\theta$.

Having satisfied (6.10), fluid columns located in region 1 and along the downstream face will be initially advected towards the ridge plateau and, as a consequence of (6.7), will acquire anticyclonic relative vorticity. Concomitantly, fluid columns in region 2 and along the upstream face will be initially advected towards the base of the ridge and, owing to (6.8), will acquire cyclonic relative vorticity. The interaction of these regions of cyclonic and anticyclonic relative vorticity induces an offshore flow along the bathymetric ridge, as observed in the laboratory experiments (see figure 13). From (6.7) and (6.8), the strength of the offshore flow and, hence, the amount of energy extracted from the –(1,1) wave during the first wave period, increases as γ decreases, which is also consistent with the experimental results reported in figure 14.

The current study demonstrates that in the absence of topography, friction acts in a complicated manner owing to the influence of rotation and is the dominant process leading to energy loss from the baroclinic basin-scale waves. A related study by Boegman, Ivey & Imberger (2005) considered the non-rotating analogue of the laboratory experiment considered here and found that nonlinear steepening of the baroclinic basin-scale wave, owing to the initial forcing and ambient stratification, resulted in the transfer of up to 20% of its energy to higher-frequency waves. The conclusion is that rotation acts, via Ekman dynamics, to damp the wave motion before significant nonlinear behaviour associated with the basin-scale wave can be observed. In this way, field observations of high-frequency waves in small stratified lakes ($S \gg 1$) (e.g. Farmer 1978; Lemmin 1987) may be generated by nonlinear steepening of the basin-scale waves; however, it is unlikely that this mechanism can account for high-frequency waves observed in large stratified lakes ($S < 1$) (e.g. Saggio & Imberger 1998; Boegman *et al.* 2003).

The addition of the topographic configurations investigated in this study provides a pathway by which energy can be rapidly removed from the basin-scale wave and transferred to an offshore flow (bathymetric ridge) or an eddy-field (cape), resulting in significant horizontal mixing between the nearshore and the interior of the basin in a relatively short period. The interaction between the $-(1,1)$ wave and the radially protruding cape, provides an explanation for the field observations of Rueda *et al.* (2003) in Lake Tahoe (USA) where it was noted that interaction between the $-(1,1)$ wave (referred to as the horizontal mode one Kelvin wave) and abrupt changes in the shoreline topography resulted in the injecting of (eddy) kinetic energy into the interior of the basin (see figure 13 in Rueda *et al.* 2003). In this way, wave/topography interactions may play a significant role in establishing the meso-scale eddy field reported by Ralph (2003) in Lake Superior (North America) and, as a consequence, such interactions may be extremely important in determining the horizontal mixing of chemical agents and biological matter within such large stratified lakes. We conclude this study by noting that it is wave/topography interactions that govern the energy pathways of baroclinic basin-scale waves in lakes influenced by the Earth's rotation and postulate that high-frequency waves observed in large stratified lakes are most probably due to wave/topography interactions.

The authors are grateful to Jason Antenucci, Roman Stocker and three anonymous referees for useful comments on initial drafts of this manuscript. G. W. acknowledges the support of an Australian Postgraduate Award and a Jean Rogerson Supplementary scholarship.

This research was funded by the Australian Research Council and forms Centre for Water Research reference ED1650-GW.

REFERENCES

Antenucci, J. P. & Imberger, J. 2001 Energetics of long internal gravity waves in large lakes. *Limnol. Oceanogr.* **46**, 1760–1773.

Boegman, L., Imberger, J., Ivey, G. N. & Antenucci, J. P. 2003 High-frequency waves in large stratified lakes. *Limnol. Oceanogr.* **48**, 895–919.

Boegman, L., Ivey, G. N. & Imberger, J. 2005 The energetics of large-scale internal wave degeneration in lakes. *J. Fluid Mech.* (submitted).

Chang, P. 1991 Coastal Kelvin waves in the presence of a slowly varying topography. *J. Fluid Mech.* **231**, 303–324.

Condie, S. A. & Ivey, G. N. 1988 Convectively driven coastal currents in a rotating basin. *J. Mar. Res.* **46**, 473–479.

Csanady, G. T. 1967 Large-scale motion in the Great Lakes. *J. Geophys. Res.* **72**, 4151–4162.

Csanady, G. T. 1973 Transverse internal seiches in large oblong lakes and marginal seas. *J. Phys. Oceanogr.* **3**, 439–447.

Farmer, D. M. 1978 Observations of long nonlinear internal waves in a lake. *J. Phys. Oceanogr.* **8**, 63–73.

Gill, A. E. 1982 *Atmosphere–Ocean Dynamics*. Academic.

Horn, D. A., Imberger, J. & Ivey, G. N. 2001 The degeneration of large-scale interfacial gravity waves in lakes. *J. Fluid Mech.* **434**, 181–207.

Horn, D. A., Imberger, J., Ivey, G. N. & Redekopp, L. G. 2002 A weakly nonlinear model of long internal waves in closed basins. *J. Fluid Mech.* **467**, 269–287.

Imberger, J. 1998 Flux paths in a stratified lake – a review. In *Physical Processes in Lakes and Oceans*, pp. 1–18. AGU Press.

Ivey, G. N. & Maxworthy, T. 1992 Mixing driven by internal Kelvin waves in large lakes and the coastal oceans. In *11th Australasian Fluid Mech. Conf. Hobart, Australia*, pp. 303–306.

Jacobs, P. & Davies, P. A. 1999 Boundary currents over shelf and slope topography. *J. Mar. Sys.* **19**, 137–158.

Killworth, P. 1989*a* How much of a coastal Kelvin wave gets over a ridge? *J. Phys. Oceanogr.* **19**, 321–341.

Killworth, P. 1989*b* Transmission of a two-layer coastal Kelvin wave over a ridge. *J. Phys. Oceanogr.* **19**, 1131–1148.

Kuo, A. C. & Polvani, L. M. 1999 Wave–vortex interaction in rotating shallow water. Part 1. One space dimension. *J. Fluid Mech.* **394**, 1–27.

Lamb, S. H. 1932 *Hydrodynamics*. Dover.

Lemmin, U. 1987 The structure and dynamics of internal waves in Baldeggersee. *Limnol. Oceanogr.* **32**, 43–61.

Martinsen, E. A. & Weber, J. E. 1981 Frictional influences on internal Kelvin waves. *Tellus* **33**, 402–410.

Melville, W. K., Tomasson, G. G. & Renouard, D. P. 1989 On the stability of Kelvin waves. *J. Fluid. Mech.* **206**, 1–23.

Pedlosky, J. 1987 *Geophysical Fluid Dynamics*. Springer.

Ralph, E. A. 2003 Scales and structures of large lake eddies. *Geophys. Res. Lett.* **29**, art. no. 2177.

Reznik, G. M. & Grimshaw, R. 2002 Nonlinear geostrophic adjustment in the presence of a boundary. *J. Fluid Mech.* **471**, 257–283.

Reznik, G. M., Zeitlin, V. & Ben Jelloul, M. 2001 Nonlinear theory of geostrophic adjustment. Part 1. Rotating shallow-water model. *J. Fluid Mech.* **445**, 93–120.

Riley, J. J. & Lelong, M.-P. 2000 Fluid motions in the presence of strong stable stratification. *Annu. Rev. Fluid Mech.* **32**, 613–657.

Rueda, F. J., Schladow, S. G. & Ó. Pálmarsson, S. 2003 Basin-scale wave dynamics during a winter cooling period in a large lake. *J. Geophys. Res.* **108** (C2), art. no. 3097.

Saggio, A. & Imberger, J. 1998 Internal wave weather in a stratified lake. *Limnol. Oceanogr.* **43**, 1780–1795.

Stocker, R. & Imberger, J. 2003 Energy partitioning and horizontal dispersion in the surface layer of a stratified lake. *J. Phys. Oceanogr* **33**, 512–529.

Stocker, R., Imberger, J. & D'Alpaos, L. 2000 An analytical model of a circular stratified rotating basin under the effect of periodic wind forcing. In *5th Intl Symp. in Stratified Flows, Vancouver, Canada*, pp. 387–392.

Tomasson, G. G. & Melville, W. K. 1990 Nonlinear and dispersive effects in Kelvin waves. *Phys. Fluids* A **2**, 189–193.

Wake, G. W., Ivey, G. N., Imberger, J. & McDonald, N. R. 2004*a* The temporal evolution of a geostrophic flow in a rotating stratified basin. *Dyn. Atmos. Oceans.* (in press).

Wake, G. W., Ivey, G. N., Imberger, J., McDonald, N. R. & Stocker, R. 2004*b* Baroclinic geostrophic adjustment in a rotating circular basin. *J. Fluid Mech.* **515**, 63–86.

Zeitlin, V., Reznik, G. M. & Ben Jelloul, M. 2003 Nonlinear theory of geostrophic adjustment. Part 2. Two-layer and continuously stratified primitive equations. *J. Fluid Mech.* **491**, 207–228.